

Ultraprecision Imaging and Manipulation of Plasmonic Nanostructures by Integrated Nanoscopic Correction

Yunbo Liu, Zhijia Zhang, Younggeun Park, and Somin Eunice Lee*

Optical manipulation and imaging of nano-objects with nanometer precision is highly desirable for nanomaterial and biological studies due to inherent noninvasiveness. However, time constraints and current segregated experimental systems for nanoimaging and nanomanipulation limits real-time super-resolution imaging with spatially enhanced manipulation. Here, an integrated nanoscopic correction (iNC) method to enable multimodal nanomanipulation-nanoimaging is reported. The iNC consists of a multimodal voltage-tunable power modulator, polarization rotator, and polarizer. Using the iNC, plasmonic nano-objects which are below the diffraction limit and which can be distinguished by direct observation without post processing are demonstrated. Furthermore, such direct observations with enhanced nanometer spatial stability and millisecond high speed are shown. Precise trapping and rapid rotation of gold nanorods with the iNC are demonstrated successfully. With non-invasive post-processing free nanoimaging and nanomanipulation, it is anticipated that the iNC will make contributions in the nanomaterial and biological sciences requiring precision optics.

with imaging would be highly desirable for enabling precise, direct delivery of nano-objects carrying editing components. Recently, super-resolution optical imaging has allowed for bypassing the diffraction limit to observe spatial features of objects with exquisite detail. Super-resolution methods increase resolution by spectral separation of fluorophores, as employed in ground state depletion microscopy, stimulated emission depletion, and reversible saturable optical fluorescence transitions.^[3–5] Super-resolution methods also commonly increase resolution by temporal separation of fluorophores, as utilized in photoactivated localization microscopy, super-resolution optical fluctuation imaging, and stochastic optical reconstruction microscopy.^[6–8] To achieve spectral and temporal separation of fluorophores, super-resolution imaging can require as many as 10^5 images, taking as

1. Introduction

Precise, direct delivery of editing components to a desired intracellular site (Figure 1) is considered to be essential for emerging precision medicine and gene editing, as editing activities must be spatially controlled to ensure efficacy.^[1] Pioneering works in optical trapping have demonstrated controlled manipulation and assembly of objects.^[2] Optical manipulation

long as several hours to acquire a complete image stack.^[6] Such time constraints, as well as segregated experimental systems, limit integration of real-time super-resolution imaging with spatially enhanced manipulation. Super-resolution imaging combined with manipulation of nano-objects is necessary to open new possibilities in nanomaterial and biological studies.


Alternatively, plasmonic nano-objects^[9–25] undergo elastic scattering processes which are energy conserving and therefore hold great potential as probes with an unlimited photon budget for real-time super-resolution. Unlike conventional super-resolution approaches using spectral and temporal separation of fluorophores, the underlying principle here utilizes anisotropic plasmonic nano-objects which can be differentiated below the diffraction limit by polarization.^[26–32] However, conventional implementations to rotate the polarization by mechanical means introduce beam deviations and subsequently result in spatial errors. When spatial errors reach the same size order as the objects-of-interest, positional information (nanometers) becomes obscured, limiting real-time super-resolution capabilities.

Here, we present an integrated nanoscopic correction method to enable multimodal nanomanipulation-nanoimaging. The iNC consists of liquid crystal and fixed retarders to function as a multimodal voltage-tunable power modulator, polarization rotator, and polarizer. Systematic voltage control enables correction of beam deviations and dynamic modulation of the transmission polarization. The transmission polarization can be rapidly tuned for dynamic, high speed nanoimaging and

Y. Liu, Z. Zhang
Department of Electrical and Computer Engineering
University of Michigan
Ann Arbor, MI 48109, USA

Dr. Y. Park
Department of Mechanical Engineering
Center for Integrative Research in Critical Care
University of Michigan
Ann Arbor, MI 48109, USA

Prof. S. E. Lee
Department of Electrical and Computer Engineering
Department of Biomedical Engineering
Biointerfaces Institute
Applied Physics
Macromolecular Science and Engineering
University of Michigan
Ann Arbor, MI 48109, USA
E-mail: sleee@umich.edu

 The ORCID identification number(s) for the author(s) of this article can be found under <https://doi.org/10.1002/smll.202007610>.

DOI: 10.1002/smll.202007610

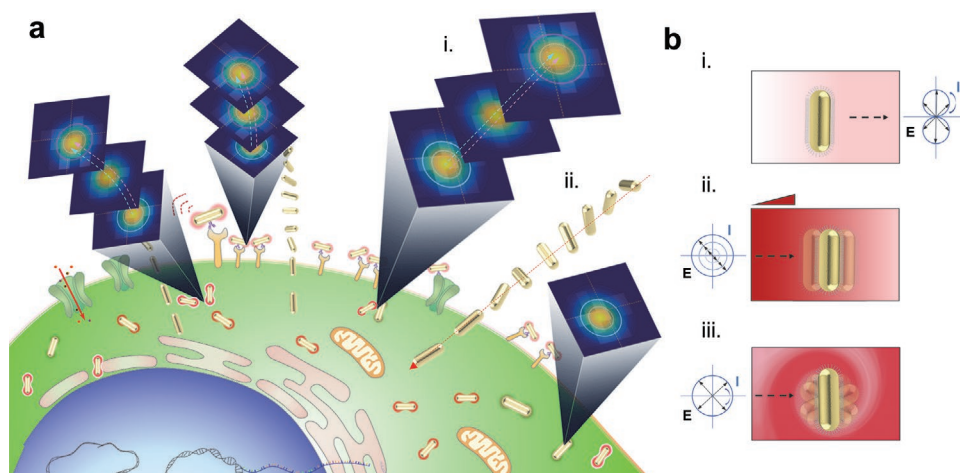


Figure 1. Ultraprecision imaging and manipulation is enabled by integrated nanoscopic correction (iNC). a) Precise delivery of nano-objects to a desired intracellular location can be enabled by real-time super resolution imaging combined with precise, active control. Spatially enhanced nanoimaging without postprocessing by the iNC allows for integration with optical manipulation (i). The iNC enables spatially enhanced nanomanipulation of nano-objects (ii). b) The iNC has multiple modes of operation. The iNC in the polarizer mode for spatially enhanced nanoimaging (i). The iNC in the power modulator mode (ii) and polarization rotator mode (iii) for spatially enhanced nanomanipulation.

nanomanipulation. We show that the iNC can be switched between different modes (power modulator, polarization rotator, and polarizer) with nanometer spatial precision. Using the iNC, we demonstrate plasmonic nano-objects (gold nanorods) which are below the diffraction limit can be distinguished by direct observation without post processing. Furthermore, we show such direct observations with nanometer spatial stability and millisecond high speed. To the best of our knowledge, for the first time, the iNC directly visualizes segregated nano-objects at the nanoscale without post-processing. We successfully demonstrate precise trapping and rapid rotation of gold nanorods with the iNC.

2. Results and Discussion

2.1. Spatially Enhanced Nanoimaging by iNC

Integrated nanoscopic correction is necessary to enable real-time super resolution imaging. For this purpose, we built a fully integrated active control system comprised of a series of liquid crystal (LC) and fixed retarders allowing for multimodal operations (Figure 2). As a first step, the iNC was operated in the polarizer mode to image plasmonic nano-objects. In this operation mode, the output Stokes parameters of the iNC can be theoretically calculated from the following Mueller matrix as

$$\begin{bmatrix} I \\ Q \\ U \\ V \end{bmatrix} = \frac{1}{2} \begin{bmatrix} 1 & -\cos \delta_1 & -\sin \delta_1 & 0 \\ -\cos \delta_2 & \cos \delta_1 \cos \delta_2 & \sin \delta_1 \cos \delta_2 & 0 \\ -\sin \delta_2 & \cos \delta_1 \sin \delta_2 & \sin \delta_1 \sin \delta_2 & 0 \\ 0 & 0 & 0 & 0 \end{bmatrix} \begin{bmatrix} I_s \\ Q_s \\ U_s \\ V_s \end{bmatrix} \quad (1)$$

$$= \frac{1}{2} \begin{bmatrix} 1 - \cos \delta_1 \\ \cos \delta_2 (\cos \delta_1 - 1) \\ \sin \delta_2 (\cos \delta_1 - 1) \\ 0 \end{bmatrix} \quad (2)$$

where $[I, Q, U, V]^T$ is the output Stokes vector, $[I_s, Q_s, U_s, V_s]^T = [1, 1, 0, 0]^T$ is the input Stokes vector of linearly polarized light, and δ_1 and δ_2 are the phase retardations of the LCs. Following Equations (1) and (2), the retardance was simulated. Theoretical results confirmed the behavior of the iNC was identical to that of a linear polarizer (Figure S2, Supporting Information). To experimentally characterize the polarizer performance, the phase retardations, δ_1 of LC₁ and δ_2 of LC₂ were controlled by applying voltages, V_{LC1} and V_{LC2} . As the phase retardations were dependent on the applied voltages, we experimentally measured the exact polarization directions at each applied voltage. The dependence of the applied voltages on the transmission polarization axis θ showed linearity from 0° to 180° (Figure 2). We then placed the iNC after a linear polarizer (Figure S4, Supporting Information). The angle α between the transmission axes of the iNC and the linear polarizer was initially set to be orthogonal. The polarizer mode was achieved by simultaneously tuning both phase retardations δ_1 and δ_2 , which depend on the applied voltages, V_{LC1} and V_{LC2} . When we tuned both V_{LC1} (3.05 to 11.9 V) and V_{LC2} (3.58 to 11.6 V) of the iNC, the transmission intensity I_{trans} was directly proportional to $\cos(2\alpha)$. Matching with Malus's law, experimental results demonstrated the iNC operation was identical to that of a linear polarizer (Figure 2). To experimentally characterize the temporal performance (Figure S5, Supporting Information), actuation voltages corresponding to perpendicular (off-state) and parallel (on-state) polarization were applied. The iNC demonstrated a rapid turn-on and -off response time of 25 and 50 ms, respectively (Figure 2), showing potential for rapid imaging. To image plasmonic nano-objects, the iNC was aligned in the detection path. As a representative model of plasmonic nano-objects, we used gold nanorods due to the asymmetric geometry and enhanced scattering as a result of the collective oscillation of electron density at the metal dielectric interface. For imaging single gold nanorods, the applied voltages V_{LC1} and V_{LC2} were rapidly modulated to switch the transmission polarization from parallel to perpendicular. As a result, the scattering intensity of a

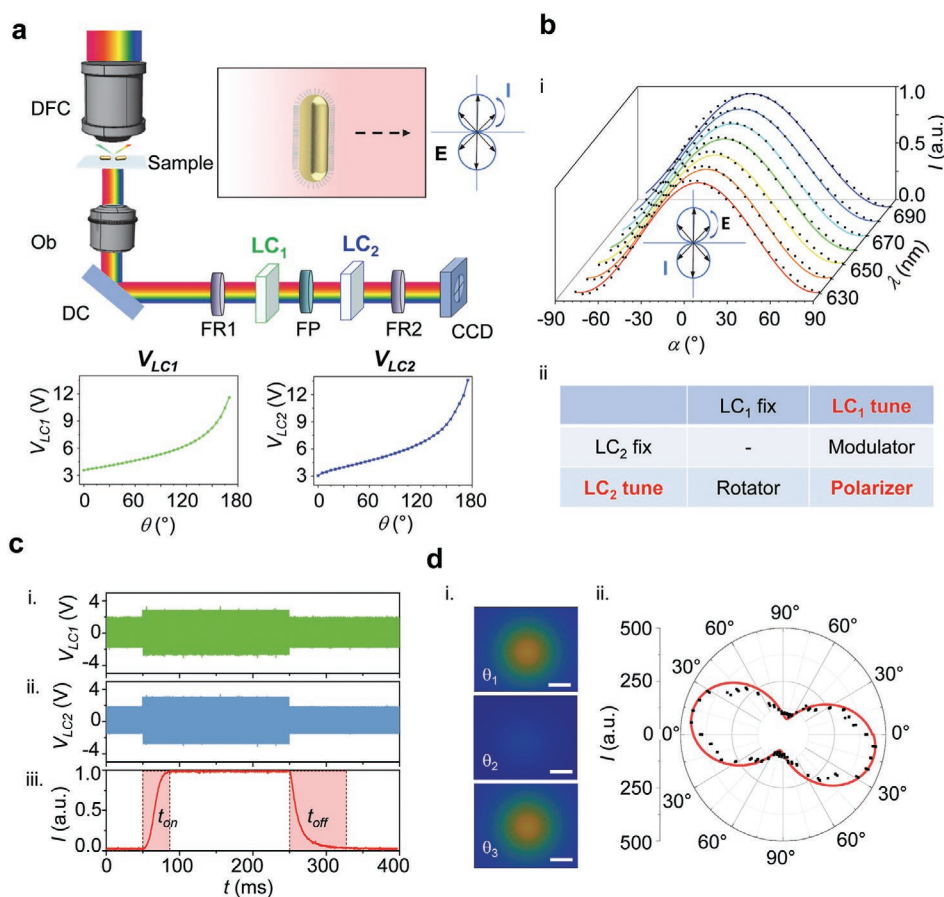


Figure 2. The iNC enables spatially enhanced nanoimaging of nano-objects. a) Conceptual schematic of the iNC integrated into a transmission dark-field microscope for nanoimaging (see Supporting Information). DFC, darkfield condenser; Ob, objective; DC, dichroic mirror; FR1, fixed retarder; LC₁, liquid crystal retarder; FP, fixed polarizer; LC₂, liquid crystal retarder; FR2, fixed retarder; CCD, charge coupled detector. b) The iNC in the polarizer mode: Transmission intensity versus angle α across wavelengths λ following Malus's Law (i). Angle α is between the transmission axes of the device and a fixed linear polarizer. The iNC operation chart showing iNC in the polarizer mode (ii). c) Graph of actuation voltage V_{LC1} for LC₁ (green) (i). Graph of actuation voltage V_{LC2} for LC₂ (blue) (ii). Graph of response time of the iNC in the polarizer mode, where t_{on} is the turn-on response time and t_{off} is the turn-off response time (iii). d) Images of a gold nanorod at varying transmission polarization using the iNC (i). Scale bar: 470 nm. Polar diagram of scattering intensity as a function of transmission polarization by the iNC at peak wavelength 650 nm (ii).

gold nanorod was periodically modulated between bright and dark states over time (Figure 2).

Spatially enhanced nanoimaging can be achieved by modulating polarization using the iNC (Figure 3). We imaged single nano-objects (gold nanorods) over a range of polarization θ from 0° to 180°. When a mechanically rotated polarizer was used to rotate the polarization from 0° to 180°, the Airy patterns of the imaged nano-objects followed a spiral trace (red curve) exhibiting a $\sin(\theta/2)$ behavior due to beam deviations arising from rotating optics. In the magnified images, a red arrow indicates its center at 175°, and a red cross-hair indicates its center at 0°. Each nano-object was displaced due to beam deviations. In contrast, the iNC corrects for beam deviations. With the iNC, we observed the Airy patterns of the imaged nano-objects followed a straight trace (blue line). For each nano-object, a blue arrow indicates its center at 175°, and a red cross-hair indicates its center at 0°, showing positions of nano-objects remained the same with the iNC. For quantitative characterization, the root-mean-square deviation (RMSD) of each pixel was calculated between the intensity of the pixels at different polarization

directions and a fitted sinusoidal function. With a mechanically rotated polarizer, large RMSD was observed due to beam deviations and subsequent loss of spatial information from finite CCD sampling. Conversely, we observed small RMSD with the iNC, indicating successful correction of beam deviations. When spatial errors (1300 nm) reach the same order of magnitude as the diameter of the Airy patterns (full width half maximum FWHM = 850 nm) as well as the pixel size (170 nm), positional information is substantially obscured and direct visualization of the proximal nano-objects from their far-field Airy patterns becomes infeasible.

Correction of beam deviations by the iNC gives rise to accurate and precise spatial information, allowing us to directly observe and distinguish segregated Airy patterns of proximal nano-objects without post image processing (Figure 3). With beam deviations corrected, a single nano-object remained at the same position as the polarization was modulated by the iNC. With beam deviations corrected for proximal nano-objects, positions of Airy patterns corresponding to positions of each nano-object emerged as the polarization was modulated by

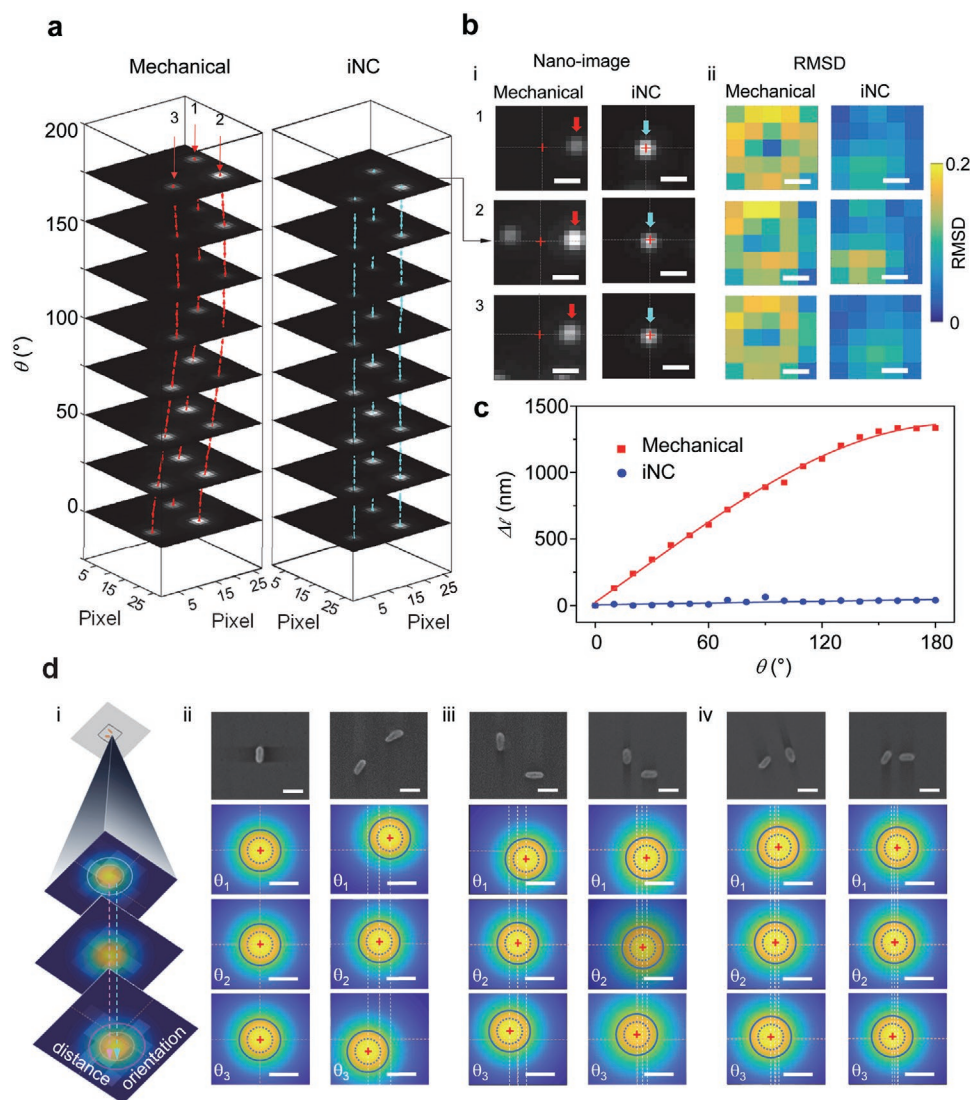


Figure 3. Nanometer spatial stability of the iNC facilitates direct observation below the diffraction limit. a) Images over transmission polarization using a conventional polarizer, and images over transmission polarization using the iNC. b) Magnified images using a conventional polarizer, and magnified images using the iNC (i). RMSD using a conventional polarizer versus the iNC. Scale bar: 1 μm (ii). c) Graph of spatial deviation over transmission polarization for a conventional polarizer versus the iNC. d) Conceptual schematic of direct observation below the diffraction limit by spatial stability of the iNC (i). SEM comparison of single versus multiple nanorods. Scale bar: 125 nm. Corresponding images over transmission polarization. Scale bar: 500 nm (ii). SEM of distance variation. Scale bar: 125 nm. Corresponding images over transmission polarization. Scale bar: 500 nm (iii). SEM of angle variation. Scale bar: 125 nm. Corresponding images over transmission polarization. Scale bar: 500 nm (iv).

the iNC. To investigate the precision of iNC, we varied the distance between proximal nano-objects and compared with measurements by scanning electron microscopy. As the distance between proximal nano-objects was varied, we directly observed distances between Airy patterns exactly corresponded to the distances measured by scanning electron microscopy (Figure S6, Supporting Information). We also varied the orientation of proximal nano-objects and found that individual Airy patterns can be directly differentiated by their far-field images, enabling positional information to be ascertained in agreement with scanning electron microscopy (Figure S6, Supporting Information). We highlight direct observations without post-processing is made possible by correcting beam deviations below the size of Airy patterns. Such direct observations have

the potential to accelerate the acquisition of super-resolution images.

2.2. Spatially Enhanced Nanomanipulation by iNC

Super-resolution imaging integrated with manipulation of nano-objects should advance dynamical studies. Optical trapping of plasmonic nano-objects has been extensively demonstrated,^[33–37] however, not in the context of real-time super-resolution. The iNC integrates trapping and manipulation of plasmonic nano-objects using the power modulator mode (Equations (3) and (4)) and polarization rotator mode (Equations (5) and (6)), respectively.

iNC power modulator

$$\begin{bmatrix} I \\ Q \\ U \\ V \end{bmatrix} = \frac{1}{2} \begin{bmatrix} 1 & -\cos \delta_1 & -\sin \delta_1 & 0 \\ 0 & 0 & 0 & 0 \\ -1 & \cos \delta_1 & \sin \delta_1 & 0 \\ 0 & 0 & 0 & 0 \end{bmatrix} \begin{bmatrix} I_s \\ Q_s \\ U_s \\ V_s \end{bmatrix} \quad (3)$$

$$= \frac{1}{2} \begin{bmatrix} 1 - \cos \delta_1 \\ 0 \\ -1 + \cos \delta_1 \\ 0 \end{bmatrix} \quad (4)$$

iNC polarization rotator

$$\begin{bmatrix} I \\ Q \\ U \\ V \end{bmatrix} = \frac{1}{2} \begin{bmatrix} 1 & 0 & -1 & 0 \\ -\cos \delta_2 & 0 & \cos \delta_2 & 0 \\ -\sin \delta_2 & 0 & \sin \delta_2 & 0 \\ 0 & 0 & 0 & 0 \end{bmatrix} \begin{bmatrix} I_s \\ Q_s \\ U_s \\ V_s \end{bmatrix} \quad (5)$$

$$= \frac{1}{2} \begin{bmatrix} 1 \\ -\cos \delta_2 \\ -\sin \delta_2 \\ 0 \end{bmatrix} \quad (6)$$

Theoretical results show the power modulation mode can be achieved in a linear regime (Figure S7, Supporting Information) while the polarization rotator mode can rotate the polarization state of light with respect to the retardance (Figure S8, Supporting Information). To experimentally demonstrate the iNC in the power modulator mode, we placed the iNC after a fixed linear polarizer and increased V_{LC1} from 3 to 5.5 V and fixed V_{LC2} at 3.3 V (Figure S9, Supporting Information). By tuning V_{LC1} , the transmission power intensity (I) changes by varying V_{LC1} at constant $V_{LC2} = 3.3$ V across a range of wavelengths λ . As I increased with V_{LC1} , a linear response was observed between $V_{LC1} = 3.8$ and 4.8 V. This consistent linear response of I was obtained regardless of the wavelength of incident light from 630 to 690 nm which allows for compatibility of the iNC with nano-objects of varying sizes and geometries. To experimentally demonstrate the iNC in the polarization rotator mode, the iNC was then positioned between two fixed linear polarizers (Figure S10, Supporting Information). To operate in the polarization rotator mode, V_{LC1} was fixed and V_{LC2} was varied. We constructed a calibration curve of polarization rotation angle ξ as a function of different voltages V_{LC2} from 3.3 to 11.4 V. The calibration curve in Figure 4b-ii was consistent across wavelength for versatility with various nano-objects.

With the iNC in the power modulation mode, beam deviations can be corrected for spatially enhanced optically trapping. We first characterized the real-time performance of the iNC in the power modulator mode. To detect the position in real-time, the iNC was placed after a quadrant position detector (Figure S11, Supporting Information) and we measured turn-on and turn-off response times of 25 and 50 ms, respectively (Figure 4c). We were able to rapidly adjust the trapping power in 50 ms, allowing for rapid optical trapping manipulation.

To optically trap plasmonic nano-objects (gold nanorods), we placed the iNC in the trapping beam path (Figure 4). Tuning V_{LC1} allowed for different trapping powers, resulting in different trapping stiffness. Using the iNC, we modulated the trapping beam power from 30 to 90 mW. To achieve highly stabilized particle trapping, the trapping force must overcome Brownian motion, since Brownian motion is dominant in solution. The position of the nano-object was measured by acquiring a distribution of positional probability using a quadrant position detector. We observed that higher trapping powers (90 mW) resulted in narrower spatial distributions, indicating more stable trapping. With beam deviations corrected, we also directly measured the spatial distribution of the positions of the nano-object as the trapping beam power was modulated from 30 to 90 mW. It can be seen that the distribution of the positions decreased as the power increased (Figure 4c, left inset). Notably, the mean positions remained the same as the trapping beam power was modulated from 30 to 90 mW (Figure 4c, right inset), showing there was no deviation of the trapping beam using the iNC. These results support successful correction of beam deviations by the iNC for spatially enhanced optical trapping. Rapid rotation of the trapped plasmonic nano-objects (gold nanorods) can be then achieved using the polarization rotator mode of the iNC. In this mode, the iNC showed a turn-on response time of 23 ms and a turn-off response time of 72 ms (Figure 4d). To rotate trapped plasmonic nano-objects, the iNC was placed in the trapping beam path. The nano-object will tend to align along the light incident polarization due to the transferring of angular momentum from the light to the nano-object. Thus, the trapped nano-object rotates following the polarization direction. By varying V_{LC2} from 3.3 to 11.4 V, the linearly polarized trapping beam changed its polarization direction, causing the trapped nano-object (gold nanorod) to rotate. Using a polarizer/analyzer technique, the intensity of scattered light from a nanorod after a fixed analyzer was recorded with CCD. We observed that the intensity was lowest when the nanocrystal rotated to the position perpendicular to the analyzer and highest when the nanocrystal fully aligned with the analyzer (Figure 4d). Taken together, these results demonstrate precise trapping and rapid rotation of plasmonic nano-objects by the iNC. The iNC could be used in other applications^[33–37] where spatially enhanced nanoimaging and nanomanipulation of plasmonic nano-objects may be beneficial.

3. Conclusion

In conclusion, we demonstrated a multimodal iNC for spatially enhanced nanoimaging and nanomanipulation. To operate the iNC in the polarizer mode, both V_{LC1} and V_{LC2} were tuned. To operate in the power modulator mode, V_{LC1} was tuned and V_{LC2} was fixed. To operate in the polarization rotator mode, V_{LC1} was fixed and V_{LC2} was tuned. We demonstrated spatially enhanced nanoimaging by the iNC. Using the iNC in the polarizer mode, we showed that correction of beam deviations enabled direct visualization of proximal plasmonic nano-objects below the diffraction limit without post-processing. Such direct observations have the potential to accelerate the acquisition of super-resolution images to allow for integration with optical manipulation. We

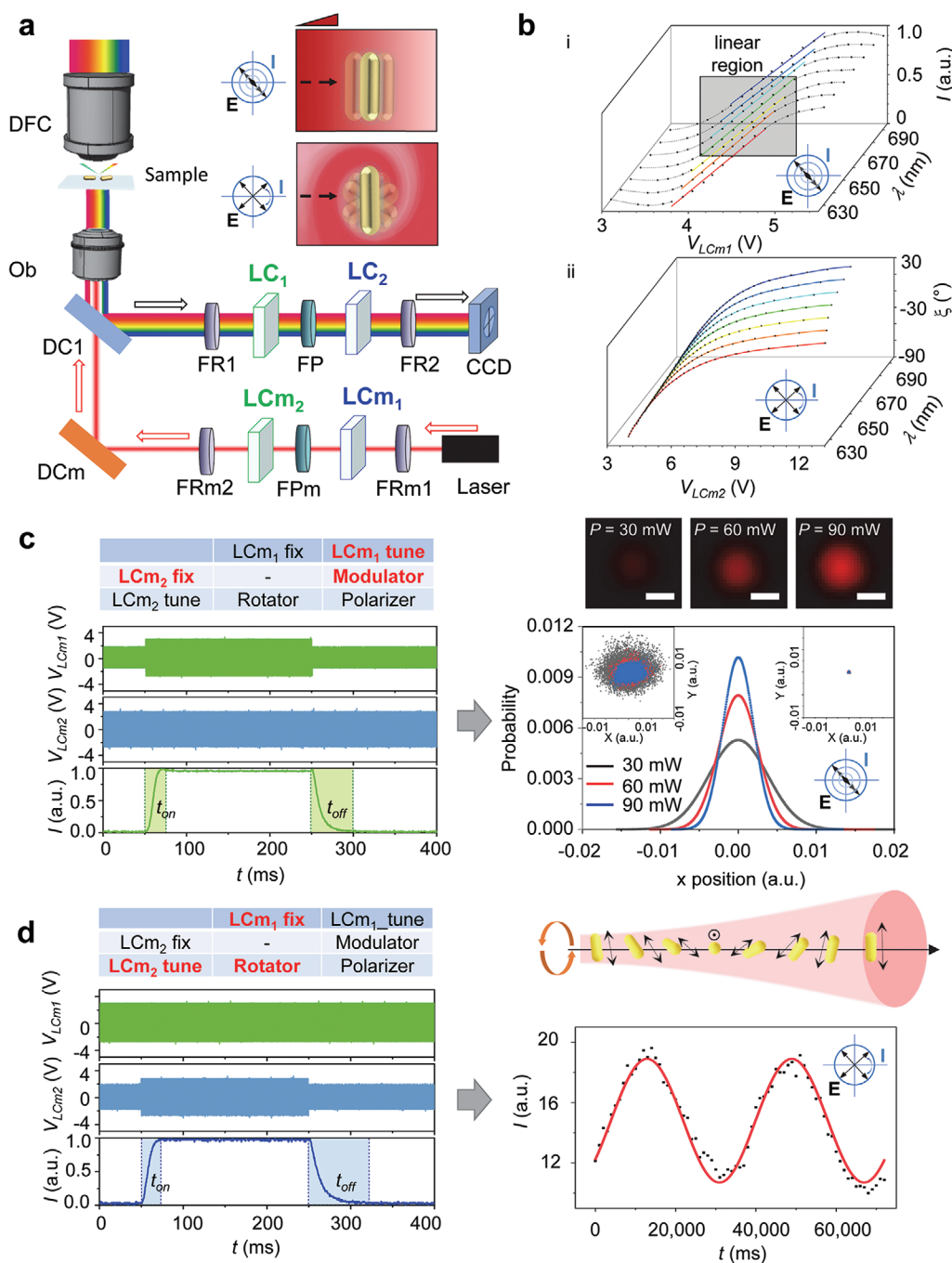


Figure 4. iNC enables spatially enhanced nanomanipulation of nano-objects. a) Conceptual schematic of the iNC integrated into a transmission dark-field microscope for nanomanipulation (see Supporting Information). DFC: darkfield condenser, Ob: objective, DC: dichroic mirror. (detection path) FR1: fixed retarder, LC₁: liquid crystal retarder, FP: fixed polarizer, LC₂: liquid crystal retarder, FR₂: fixed retarder, CCD: charge coupled detector. (trapping beam path) FRm₁: fixed retarder, LCm₁: liquid crystal retarder, FPm: fixed polarizer, LCm₂: liquid crystal retarder, FRm₂: fixed retarder. b) The iNC in power modulation mode: Graph of transmission intensity as a function of actuation voltage V_{LCm1} across wavelengths λ (i). The iNC in the polarization rotator mode: Graph of polarization rotation angle ξ as a function of actuation voltage V_{LCm2} across wavelengths λ (ii). c) The iNC operation chart showing the iNC in the power modulation mode (left). Graphs of actuation voltage V_{LCm1} for LCm₁ (green) and actuation voltage V_{LCm2} for LCm₂ (blue). Graph of response time of the iNC in the power modulation mode, where t_{on} is the turn-on response time and t_{off} is the turn-off response time. Images of the trapping beam as power P was modulated from 30 to 90 mW by the iNC (right). Probability of spatial position of a trapped nanorod measured using QPD as power P was modulated by the iNC. Scale bar: 620 nm. Left inset shows distribution of the positions decreases as power increases. Right inset shows mean positions at each power level overlap. d) The iNC operation chart showing the iNC in the polarization rotator mode (left). Graphs of actuation voltage V_{LCm1} for LCm₁ (green) and actuation voltage V_{LCm2} for LCm₂ (blue). Graph of response time of the iNC in the polarization mode, where t_{on} is the turn-on response time and t_{off} is the turn-off response time. Conceptual schematic showing the iNC rotates the polarization direction of the linearly polarized trapping beam, and the resulting trapped nanorod rotates following the polarization direction (right). Graph of scattering intensity of a rotating nanorod over time.

demonstrated spatially enhanced nanomanipulation by the iNC. Using the iNC in the power modulator mode and polarization rotator mode, we showed that correction of beam deviations resulted in precise trapping and rapid rotation of plasmonic nano-objects. This method can be applied to any nano-object exhibiting polarization anisotropy. In the future, the iNC can be applied to nano-objects of a variety of materials^[13,38,39] and geometries.^[40–42] This work opens the way for real-time super-resolution imaging integrated with active control.

4. Experimental Section

Nanoimaging: A darkfield microscope (IX73, Olympus) was configured with a dry condenser (U-DCD, Olympus), a 50× objective (LMPLFLN50XBD, Olympus), a CCD camera (ORCA II, Hamamatsu), and the iNC (Supporting Information) in the detection path. Both V_{LC1} and V_{LC2} were tuned from 3.05 to 11.9 V and from 3.3 to 11.4 V synchronously to modulate the polarization from 0° to 175° in 5° increments. An image was taken at each increment.

For comparison, a linear polarizer (LPVISE200-A, Thorlabs) was placed between the output of the microscope and the camera as a standard, mechanical case. The linear polarizer was manually rotated 180° in 5° increments. An image was taken at each increment.

The images were taken at the same transmission polarization angles. In both cases, the CCD camera was placed ≈50 mm after the optical elements. The location of the nanorod (center of the Gaussian beam) on the images was determined by Trackmate in ImageJ Fiji.^[43,44] The tracking detector was set to be LOG (Laplacian of Gaussian) for Gaussian beam detection.

The iNC was actuated automatically using a function generator (Instek, AFG2225) and DAQ board (NI, PCI6733) with periodically changing voltage levels. Each actuation period consisted of 25 voltage levels (3.05 to 11.9 V and 3.3 to 11.4 V) corresponding to polarization angles from 0° to 170° with 7° intervals. For a single period, each voltage level lasted 250 ms.

Nanomanipulation: An optical trapping system was configured with a 830 nm cw Ti:Sapphire laser (Spectra Physics 3900s) and a darkfield microscope (Olympus IX73) outfitted with a 60× water immersion objective (Olympus LUCPLFLN60XPH) and the iNC in the illumination path. With the iNC in the power modulation mode, the position of an optically trapped gold nanorod (100 nm × 30 nm) was measured by placing a QPD (PDQ80A, Thorlabs) at the conjugate back focal plane of the objective. The spatial position was measured at three different transmission powers (30, 60, and 90 mW) before the beam entered the objective. The spatial position probability function was calculated by fitting the measured voltages to a probability density function, followed by integration over a finite step size.

With the iNC in the polarization rotator mode, single gold nanorods (100 nm × 30 nm) suspended in water were trapped using the optical trapping system. By applying V_{LC2} from 3.3 to 11.4 V while V_{LC1} was held constant at 3.3 V, the polarization rotation angle was rotated from 0° to 175° repeatedly to rotate the nanorod (two cycles lasting ≈72 s). A fixed linear polarizer was placed at the detection port of the microscope to modulate the gold nanorod intensity to avoid depolarization effects at the sample plane.^[45,46] The scattering signal of the nanorod was then captured by a CCD (Thorlabs 1645C). The intensity of the nanorod at different rotational orientations was obtained by averaging the center pixels of the nanorod images with an ROI slightly larger than the FWHM of the Gaussian pattern.

Supporting Information

Supporting Information is available from the Wiley Online Library or from the author.

Acknowledgements

This work was supported by the National Science Foundation (NSF 1454188), Air Force Office of Scientific Research (AFOSR FA9550-16-1-0272, FA9550-19-1-0186), and academic research fund at the University of Michigan.

Conflict of Interest

The authors declare no conflict of interest.

Data Availability Statement

The data that support the findings of this study are available from the corresponding author upon reasonable request.

Keywords

multimodal optical trapping, multimodal super-resolution imaging, plasmonics

Received: December 4, 2020

Revised: February 12, 2021

Published online: April 15, 2021

- [1] S. Tong, B. Moyo, C. M. Lee, K. Leong, G. Bao, *Nat. Rev. Mater.* **2019**, 4, 726.
- [2] O. M. Maragò, P. H. Jones, P. G. Gucciardi, G. Volpe, A. C. Ferrari, *Nat. Nanotechnol.* **2013**, 8, 807.
- [3] T. A. Klar, S. W. Hell, *Opt. Lett.* **1999**, 24, 954.
- [4] S. W. Hell, M. Kroug, *Appl. Phys. B: Lasers Opt.* **1995**, 60, 495.
- [5] M. Hofmann, C. Eggeling, S. Jakobs, S. W. Hell, *Proc. Natl. Acad. Sci. U. S. A.* **2005**, 102, 17565.
- [6] E. Betzig, G. H. Patterson, R. Sougrat, O. W. Lindwasser, S. Olenych, J. S. Bonifacino, M. W. Davidson, J. Lippincott-Schwartz, H. F. Hess, *Science* **2006**, 313, 1642.
- [7] M. J. Rust, M. Bates, X. Zhuang, *Nat. Methods* **2006**, 3, 793.
- [8] T. Dertinger, R. Colyer, G. Iyer, S. Weiss, J. Enderlein, *Proc. Natl. Acad. Sci. U. S. A.* **2009**, 106, 22287.
- [9] C. Sönnichsen, A. P. Alivisatos, *Nano Lett.* **2005**, 5, 301.
- [10] P. Zijlstra, J. W. M. Chon, M. Gu, *Nature* **2009**, 459, 410.
- [11] W. K. Lin, G. Cui, Z. Burns, X. Zhao, Y. Liu, Z. Zhang, Y. Wang, X. Ye, Y. Park, S. E. Lee, *Adv. Mater. Interfaces* **2021**, 8, 2001370.
- [12] E. Murphy, Y. Liu, D. Krueger, M. Prasad, S. E. Lee, Y. Park, *Small* **2021**, 17, 2006044.
- [13] M. W. Knight, L. Liu, Y. Wang, L. Brown, S. Mukherjee, N. S. King, H. O. Everitt, P. Nordlander, N. J. Halas, *Nano Lett.* **2012**, 12, 6000.
- [14] J. Perez-Juste, B. Rodriguez-Gonzalez, P. Mulvaney, L. M. Liz-Marzan, *Adv. Funct. Mater.* **2005**, 15, 1065.
- [15] X. Huang, I. H. El-Sayed, W. Qian, M. A. El-Sayed, *Nano Lett.* **2007**, 7, 1591.
- [16] G. Wang, W. Sun, Y. Luo, N. Fang, *J. Am. Chem. Soc.* **2010**, 132, 16417.
- [17] W.-S. Chang, J. W. Ha, L. S. Slaughter, S. Link, *Proc. Natl. Acad. Sci. U. S. A.* **2010**, 107, 2781.
- [18] G. L. Liu, Y. T. Long, Y. Choi, T. Kang, L. P. Lee, *Nat. Methods* **2007**, 4, 1015.
- [19] S. E. Lee, G. L. Liu, F. Kim, L. P. Lee, *Nano Lett.* **2009**, 9, 562.

- [20] S. E. Lee, D. Y. Sasaki, T. D. Perroud, D. Yoo, K. D. Patel, L. P. Lee, *J. Am. Chem. Soc.* **2009**, *131*, 14066.
- [21] S. E. Lee, D. Y. Sasaki, Y. Park, R. Xu, J. S. Brennan, M. J. Bissell, L. P. Lee, *ACS Nano* **2012**, *6*, 7770.
- [22] S. E. Lee, Q. Chen, R. Bhat, S. Petkiewicz, J. M. Smith, V. E. Ferry, A. L. Correia, A. P. Alivisatos, M. J. Bissell, *Nano Lett.* **2015**, *15*, 4564.
- [23] Y. Liu, Y. Park, S. E. Lee, *Appl. Phys. Lett.* **2016**, *109*, 013109.
- [24] S. E. Lee, L. P. Lee, *Curr. Opin. Biotech.* **2010**, *24*, 489.
- [25] S. E. Lee, L. P. Lee, *Curr. Opin. Chem. Biol.* **2010**, *14*, 623.
- [26] C. L. Nehl, H. Liao, J. H. Hafner, *Nano Lett.* **2006**, *6*, 683.
- [27] O. Schubert, J. Becker, L. Carbone, Y. Khalavka, T. Provalska, I. Zins, C. Sönnichsen, *Nano Lett.* **2008**, *8*, 2345.
- [28] A. S. Stender, G. Wang, W. Sun, N. Fang, *ACS Nano* **2010**, *4*, 7667.
- [29] Q. Liu, Y. Cui, D. Gardner, X. Li, S. He, I. I. Smalyukh, *Nano Lett.* **2010**, *10*, 1347.
- [30] X. Cheng, D. Dai, D. Xu, Y. He, E. S. Yeung, *Anal. Chem.* **2014**, *86*, 2303.
- [31] K. H. Möller, I. Trabjerg, *Infrared Phys. Technol.* **2005**, *46*, 351.
- [32] D. Clarke, *Stellar Polarimetry*, Wiley, Weinheim, Germany **2010**, pp. 139–173.
- [33] S. E. S. Spesvytseva, K. Dholakia, *ACS Photonics* **2016**, *3*, 719.
- [34] J. Berthelot, S. S. Aćimović, M. L. Juan, M. P. Kreuzer, J. Renger, R. Quidant, *Nat. Nanotechnol.* **2014**, *9*, 295.
- [35] L. Shao, Z. J. Yang, D. Andrén, P. Johansson, M. Käll, *ACS Nano* **2015**, *9*, 12542.
- [36] K. C. Toussaint, M. Liu, M. Pelton, J. Pesic, M. J. Guffey, P. Guyot-Sionnest, N. F. Scherer, *Opt. Express* **2007**, *15*, 12017.
- [37] Y. Y. Tanaka, P. Albella, M. Rahmani, V. Giannini, S. A. Maier, T. Shimura, *Sci. Adv.* **2020**, *6*, eabc3726.
- [38] L. Zhang, L. T. Røling, X. Wang, M. Vara, M. Chi, J. Liu, S.-I. Choi, J. Park, J. A. Herron, Z. Xie, M. Mavrikakis, Y. Xia, *Science* **2015**, *6246*, 412.
- [39] R. Jin, Y. C. Cao, E. Hao, G. S. Metraux, G. C. Schatz, C. A. Mirkin, *Nature* **2003**, *425*, 487.
- [40] H.-E. Lee, H.-Y. Ahn, J. Mun, Y. Y. Lee, M. Kim, N. H. Cho, K. Chang, W. S. Kim, J. Rho, K. T. Nam, *Nature* **2018**, *556*, 360.
- [41] K. Chandra, K. S. B. Culver, S. E. Werner, R. C. Lee, T. W. Odom, *Chem. Mater.* **2016**, *28*, 6763.
- [42] S. E. Lohse, N. D. Burrows, L. Scarabelli, L. M. Liz-Marzán, C. J. Murphy, *Chem. Mater.* **2014**, *26*, 34.
- [43] J. Schindelin, C. T. Rueden, M. C. Hiner, K. W. Eliceiri, *Mol. Reprod. Dev.* **2015**, *82*, 518.
- [44] J.-Y. Tinevez, N. Perry, J. Schindelin, G. M. Hoopes, G. D. Reynolds, E. Laplantine, S. Y. Bednarek, S. L. Shorte, K. W. Eliceiri, *Methods* **2017**, *115*, 80.
- [45] J. B. Lassiter, J. Aizpurua, L. I. Hernandez, D. W. Brandl, I. Romero, S. Lal, J. H. Hafner, P. Nordlander, N. J. Halas, *Nano Lett.* **2008**, *8*, 1212.
- [46] M. Atakhorrami, K. M. Addas, C. F. Schmidt, *Rev. Sci. Instrum.* **2008**, *79*, 043103.